Interface Control of Semiconducting Metal Oxide Layers for Efficient and Stable Inverted Polymer Solar Cells with Open-Circuit Voltages over 1.0 Volt

Zhigang Yin, Qingdong Zheng,* Shan-Ci Chen, and Dongdong Cai

State Key Laboratory of Structural Chemistry, Fujian Institute of Research on the Structure of Matter, Chinese Academy of Sciences, 155 Yangqiao West Road, Fuzhou, Fujian 350002, P. R. China

Ⓢ Supporting Information

ABSTRACT: Inverted polymer solar cells (PSCs) with high open-circuit voltages of 1.00−1.06 V are fabricated by using an indenofluorene-containing copolymer (PIFTBT8) as an electron donor material and [6,6]-phenyl-C71-butyric acid methyl ester ($PC_{71}BM$) as an electron acceptor material. To improve the photovoltaic performance, interface control of various low-temperature processed ZnO films as cathode buffer layers is systematically investigated for effective electron transportation, while transition metal oxides including MoO_3, WO_3, NiO, and Cu_2O are employed as anode buffer layers for hole-extraction. Incorporation of optimized semiconducting metal oxide interlayers can minimize interfacial power losses, which thus affords large open-circuit voltages (V_{oc}), increased short-circuit current densities (J_{sc}), and fill factors (FF), eventually contributing to higher power conversion efficiencies (PCEs) as well as better device stability. Due to the improved interfacial contacts and fine-matching energy levels, inverted PSCs with a device configuration of $ITO/ZnO/PIFTBT8:PC_{71}BM/MoO_3/Ag$ exhibit a high PCE of 5.05% with a large V_{oc} of 1.04 V, a J_{sc} of 9.74 mA cm^{-2}, and an FF of 50.1%. For the single junction inverted PSCs with efficiencies over 5.0%, 1.04 V is the largest V_{oc} ever achieved. By controlling the processing conditions of the active layer, the V_{oc} can further be improved to 1.05 and 1.06 V, with PCEs of 4.70% and 4.18%, respectively. More importantly, the inverted PSCs are ascertained to maintain a PCE of 4.55% (>90% of its initial efficiency) and a V_{oc} of 1.05 V over 180 days, demonstrating good long-term stability, which is much better than that of the conventional devices. The results suggest that the interface engineering of metal oxide interlayers is an important strategy to develop PSCs with good performance.

KEYWORDS: inverted polymer solar cells, metal oxides, interface engineering, high open-circuit voltages, device stability
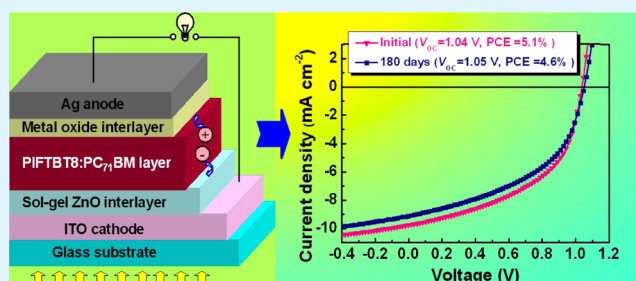
INTRODUCTION

Photovoltaics has been recognized as one of the most significant advanced technologies to collect energy from the sun for meeting the growing demand of clean and renewable resources.[1,2] Amongst various photovoltaic devices, organic polymer solar cells (PSCs) have received increasing attention over the past decade due to their salient advantages of lightness, flexibility, cost-effective fabrication, and the possibility of large-area solution processing or roll-to-roll manufacturing.[3−8] Organic PSCs with power conversion efficiencies (PCEs) approaching 10% have been recently achieved,[9−15] which promises them a bright future in low-cost solar cells compared to the currently dominant silicon-based solar cells.[16] In most PSCs, a hole transporting conjugated polymer and an electron transporting fullerene derivative are blended together to form a bicontinuous bulk-heterojunction (BHJ) layer with nanoscale phase separation.[17] It thus can provide a large interfacial area between electron donor and electron acceptor phases for efficient exciton dissociation and carrier transportation to the electrodes.[18,19] To obtain high efficiency PSCs, it is extremely important to have strong absorption of sunlight and effective charge separation/transportation within the interpenetrating networks, which can be improved by the innovation of photovoltaic materials as well as device architectures.

Conventional PSC devices generally comprise a bottom transparent conductive anode (i.e., indium tin oxide, ITO), a photoactive BHJ layer, a low work-function metal cathode (e.g., Al, Ca), and the anode/cathode interface layers. However, this device configuration suffers from poor ambient stability because the low work-function cathode is susceptible to degradation by moisture and oxygen. Meanwhile, the typical anode buffer layer, poly(3,4-ethylenedioxythiophene):poly(styrene sulfonate) (PEDOT:PSS) is of an acidic nature, which results in degradation of the device performance induced by a reaction between the electrode and PEDOT:PSS.[20,21] The instability of conventional PSCs is now one of the main problems to be tackled before

actual application of PSCs. One good strategy to improve the stability of PSCs is to adopt an inverted device structure wherein the polarity of the charge collecting electrodes is reversed. In the inverted device configuration, modified-ITO substrates are used as transparent cathodes to collect electrons, and high work-function metals (e.g., Ag, Au) are usually employed as the air-stable anodes to collect holes, thus contributing to the improved device stability compared to conventional PSCs.[22] So far, many efforts on high performance inverted PSCs have been made, which include the optimization of phase-separated morphologies in the BHJ layer, the utilization of newly synthesized donor or acceptor materials, and the selection of novel electrodes.[20,23−25] At the same time, interface engineering on inverted PSCs is also quite significant for improving the device efficiency and stability.[26−32] With incorporation of suitable electrode buffer layer materials as well as an optimization in interface processing in inverted PSCs, the highest PCE for single junction device reported to date is 9.2%.[11,33,34]

For inverted PSCs, the influence of electrical contacts at different interfaces plays an essential role in determining device characteristics such as open-circuit voltage (V_{oc}), short-circuit current density (J_{sc}), fill factor (FF), series resistance (R_s), and shunt resistance (R_{sh}), as well as the final device efficiency.[35−37] The R_s is decided by the bulk conductivity of each layer as well as the contact resistance of the interface between different layers in the device, while the R_{sh} can be ascribed to the quality of all the layers and their interfaces.[38,39] A low efficiency device often has large R_s and small R_{sh}, which are originated from loss of charge carriers through the leakage and the carrier trapping or recombination, from the existence of dark currents, or from the Schottky barriers formed at the interfaces.[40] Without interface engineering, poor Ohmic contacts are always generated at both interfaces between the BHJ layer and the electrodes, due to the mismatch of energy levels and the presence of interfacial defects or unfavorable dipoles.[37] Bad interfacial effects are harmful for producing a high J_{sc} and a maximum V_{oc} in theory. Accordingly, a control over the interfaces between the BHJ layer and the electrodes is critical. Using electrode interface materials with good charge-transporting ability for favorable Ohmic contacts at the interfaces is required to obtain the large V_{oc}, J_{sc}, and FF. Meanwhile, good work-function matching of the interlayer modified cathode and anode to the lowest unoccupied molecular orbital (LUMO) of the acceptor and the highest occupied molecular orbital (HOMO) of the donor, respectively, is also needed in order to maximize the V_{oc}. To achieve these goals, various semiconducting cathode/anode interfacial films have been developed as effective charge (electrons or holes) extracting and transporting layers in high performance inverted PSCs.[27,41,42]

Among the interface materials, semiconducting transition metal oxides are attractive and promising because of their solution processability as well as their outstanding capability to extract/transfer carriers.[37,43] The uses of transition metal oxides as interfacial materials can improve the performance of inverted PSCs owing to their merits of better stability, higher optical transparency, and stronger charge-transporting capabilities than those interface materials of alkali metal compounds,[26] organic conducting polymers and polyelectrolytes.[20,28−32,34,44] Zinc oxide (ZnO) is one of the best semiconducting interface materials, which has been extensively employed in inverted PSCs as an electron-transporting and hole-blocking cathode

interlayer material.[11,33,34,45] Most ZnO interface layer-based PSCs ustilized the P3HT:PCBM system as the active layer. Nonetheless, the device efficiencies of this BHJ system are largely limited by the small V_{oc} of ∼0.6 V due to the relatively large band gap of P3HT and relatively small energetic difference between the HOMO of P3HT and the LUMO of PCBM. As we pointed in our recent perspective article,[45] in order to achieve a larger V_{oc} and a higher PCE, the future stable inverted PSCs will go to the BHJ systems made by other low-band gap polymers instead of P3HT. With ZnO cathode interface layers, inverted PSCs based on different low-band gap polymers blended with fullerene derivatives have recently been demonstrated to have large V_{oc} values up to 0.8−0.9 V and high PCEs of 4−7%.[23,28−30] For real commercial products, stable PSCs with V_{oc} approaching or exceeding 1.10 V are desirable. Nevertheless, to the best of our knowledge, single junction inverted PSCs with PCEs over 5% and V_{oc} up to 1.04 V have not been achieved yet. Therefore, there is a need to systematically investigate the interface engineering of metal oxide interlayers for attaining high performance inverted PSCs with an increased V_{oc} and an improved PCE, as well as good device stability.

The motivation of this work is to realize efficient, stable inverted PSCs with high open-circuit voltages (>1.0 V) by interface controlling low-temperature processed sol−gel ZnO cathode buffer layers as well as transition metal oxide anode buffer layers such as MoO_3. One of indenofluorene-based copolymers with a deep-lying HOMO energy level[46] was blended with $PC_{71}BM$ for our proposed inverted BHJ PSCs. Incorporation of energy level-matched metal oxide interfacial layers between the BHJ layer and the electrodes can minimize interfacial power losses, provide good interface contacts, thus affording large R_{sh} and small R_s as well as efficient charge extraction/transportation, which are beneficial for improving the solar cell characteristics and ambient stabilities. Under an optimized condition, the inverted PSCs exhibit the maximum PCE of 5.05% with a large V_{oc} of 1.04 V under the illumination of AM 1.5 G, 100 mW cm^{-2}. More importantly, the inverted device shows good long-term stability, where the normalized PCE can maintain more than 90% over half a year and the high V_{oc} of 1.04−1.05 V is retained. The improved stability of the inverted devices is demonstrated to be much better than that of the corresponding PSCs with a conventional device configuration.

■ EXPERIMENTAL SECTION

Materials. An indenofluorene-containing copolymer, PIFTBT8 (molecular weight, $M_w \approx 60600$; polydispersity index, PDI ≈ 1.8) was synthesized according to the previously reported method,[46] and $PC_{71}BM$ (99%) was purchased from Solenne BV (Netherlands). Zinc acetate dihydrate (99.9%), 2-methoxyethanol (99.8%), and ethanolamine (99.5%) were purchased from Sigma-Aldrich Inc. Transition metal oxides including MoO_3 (99.9%), WO_3 (99.9%), NiO (99.9%), and Cu_2O (99.5%) were purchased from Sigma-Aldrich Inc. or Adamas-beta Ltd. and used as received. The materials and reagents were used without purification.

Preparation and Characterization of ZnO Films. Low-temperature solution processed ZnO films were fabricated on patterned ITO glasses (∼15 Ω sq^{-1}) by a facile sol−gel method. Firstly, the ITO glasses were cleaned by ultrasonication sequentially in detergent, water, acetone, and isopropyl alcohol for 30 min each and then dried at 130 °C overnight in an oven. Then the ZnO precursor solutions with different concentrations (0.10, 0.23, 0.46, and 0.70 M in 2-methoxyethanol) were spin-coated on the top of the ITO-glasses, which were pretreated by oxygen plasma for 5 min. The films were first

annealed on a hot plate at 150 °C for 10 min. The samples were further transferred into an oven and annealed at 200 °C for 1 h in air. UV-vis transmission measurements of ZnO films deposited on ITO glasses were recorded at room temperature with a Lambda35 spectrophotometer. Atomic force microscopy (AFM) images were obtained by a Veeco Multimode NS3A-02 Nanoscope III atomic force microscope. X-ray diffraction (XRD) patterns were performed on a Rigaku Miniflex II diffractometer (Cu Kα radiation, 30 kV, 15 mA). The thicknesses of ZnO films were determined by a Bruker Dektak XT surface profiler.

Fabrication and Measurements of ZnO Thin-Film Field-Effect Transistors (FETs). All FET devices based on n-type ZnO were fabricated on SiO_2/Si wafers without any surface treatment. The ZnO films were deposited on SiO_2/Si by the same procedure as that used for the ZnO films on ITO glass. Top-contact source/drain Al electrodes of about 100 nm thickness were vapor-deposited through a shadow mask under a vacuum of $\sim 1 \times 10^{-4}$ Pa. The channel width (W) and length (L) were 6.0 mm and 300 μm, respectively. All fabricated FET devices were tested in air using an Agilent semiconductor parameter analyzer (Agilent 4155C) with the ICS lite software for calculating the carrier mobility of ZnO films. The mobilities are calculated from transfer characteristic curves using the slope derived from the square root of absolute value of the current as a function of gate voltage between 30 and 50 V.

Fabrication and Measurements of PSCs. Inverted PSCs were prepared on the ZnO-coated ITO glasses. At first, the ITO-glass substrates coated with ZnO films as cathode interfacial layers were transferred into a glove box. Then, an active layer was fabricated in the glove box by spin-casting a blend of PIFTBT8:PC_{71}BM in a 1:4 (by weight) ratio on the ZnO/ITO substrates, followed by heating at 80 °C for 10 min. Then, the devices were kept at room temperature for 24 h. Finally, an anode interfacial layer of MoO_3 and the electrode (Ag, 100 nm) were deposited on top of the active layer through shadow masks by thermal evaporation under a high vacuum ($\sim 3 \times 10^{-5}$ Pa). For some devices, hole-injecting WO_3, NiO, and Cu_2O films were also thermally evaporated and controlled as anode buffer layers to replace the MoO_3 interlayer. In addition, conventional PSCs were also fabricated so as to have a comparison with the inverted PSCs. Firstly, a thin layer of spin-coated PEDOT:PSS (Baytron PAl 4083, $\sim$40 nm) or thermally-evaporated MoO_3 (10 nm) was covered on the ITO surface. Then, the PEDOT:PSS/ITO glasses were dried at 130 °C for 30 min (without this treatment for MoO_3/ITO-glasses). The same BHJ layer was spin-coated on the prepared substrates by the same conditions as that for the inverted PSCs. Then the devices were also kept at room temperature for 24 h. Later, 10 nm of Ca (or 1 nm of LiF) and 100 nm of Al were deposited through shadow masks by thermal evaporation under a vacuum of $\sim 1 \times 10^{-4}$ Pa. The active area of all the inverted and conventional devices was fixed at 6 mm^2. The PIFTBT8 and PC_{71}BM were dissolved in a mixture of o-dichlorobenzene and chorobenzene (1:4 by volume) to give an overall 20 mg/mL solution. Solar cell characterization was performed under AM 1.5 G irradiation (100 mW cm^{-2}) from an Oriel Sol3A simulator (Newport) with a NREL-certified silicon reference cell. After a simple encapsulation by epoxy kits (general purpose, Sigma Aldrich) in the glove-box, the PSCs were illuminated through their ITO sides. Current density−voltage (J−V) curves were tested in air by a Keithley 2440 source measurement unit. External quantum efficiency (EQE) spectra for the inverted PSCs were measured on a Newport EQE measuring system.

■ RESULTS AND DISCUSSION

Materials and Device Configuration. In this work, one of our BHJ material systems developed by Zheng et al.[46] was chosen, and different transition metal oxide semiconductors were explored as cathode and anode interfacial layers for efficient charge extraction/transportation. The inverted device structure employs the ladder-type indenofluorene-containing copolymer (PIFTBT8) as a donor material and the PC_{71}BM as an acceptor material in the BHJ active layer (Figure 1a and b). n-Type semiconducting ZnO films are sandwiched between the
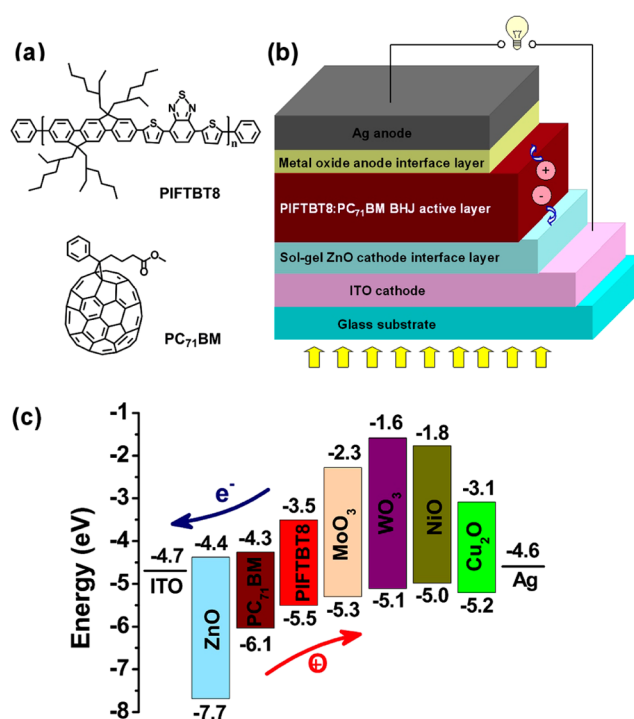

Figure 1. (a) Molecular structures of PIFTBT8 and PC_{71}BM, (b) a schematic device structure of inverted PSCs based on PIFTBT8:PC_{71}BM, and (c) energy levels of materials used in the inverted PSCs with semiconducting ZnO as the cathode interfacial layer and various transition metal oxides as the anode interfacial layers.

active layer and ITO as the cathode interface layer for electron transportation, and various transition metal oxides (MoO_3, WO_3, NiO, or Cu_2O) with hole-injecting semiconductor characteristics are inserted between the Ag and the BHJ layer as the anode interfacial layer for hole extraction. The relevant energy levels of all materials used in the inverted solar cells based on PIFTBT8:PC_{71}BM are shown in Figure 1c. Although there have been many reports on binary transition metal oxides, few in-depth investigations are related to the influence of their band structure, band-gap (E_g), valence band maximum (VBM), conduction band minimum (CBM), work function etc. on the organic photovoltaic device performance.[36,37] Here, we present an overall study of metal oxide interfacial layers in PSCs especially in highly efficient and stable inverted PSCs. Corresponding discussions of the energy level orderings associated with various inverted solar cells based on PIFTBT8:PC_{71}BM are illustrated in the following sections.

Optimization of ZnO Cathode Interfacial Layers to Improve Device Performance. Low-temperature solution-processed ZnO cathode interfacial layers were fabricated on ITO-glasses by a facile sol−gel method, and the synthetic details are described in the Experimental Section. After annealing at 200 °C for 1 h, the precursor sols was converted to dense ZnO films through a hydrolysis process.[28,47] To investigate the influence of ZnO interfacial layers on the performance of the inverted solar cells based on PIFTBT8:PC_{71}BM, a series of thin ZnO films are fabricated by controlling the concentration of ZnO precursor solutions. By using ZnO precursors with the concentrations of 0.10, 0.23, 0.46, and 0.70 M, the corresponding film thicknesses are determined to be approximately 7, 15, 29, and 54 nm, respectively. The formed ZnO layer shows an increase in film
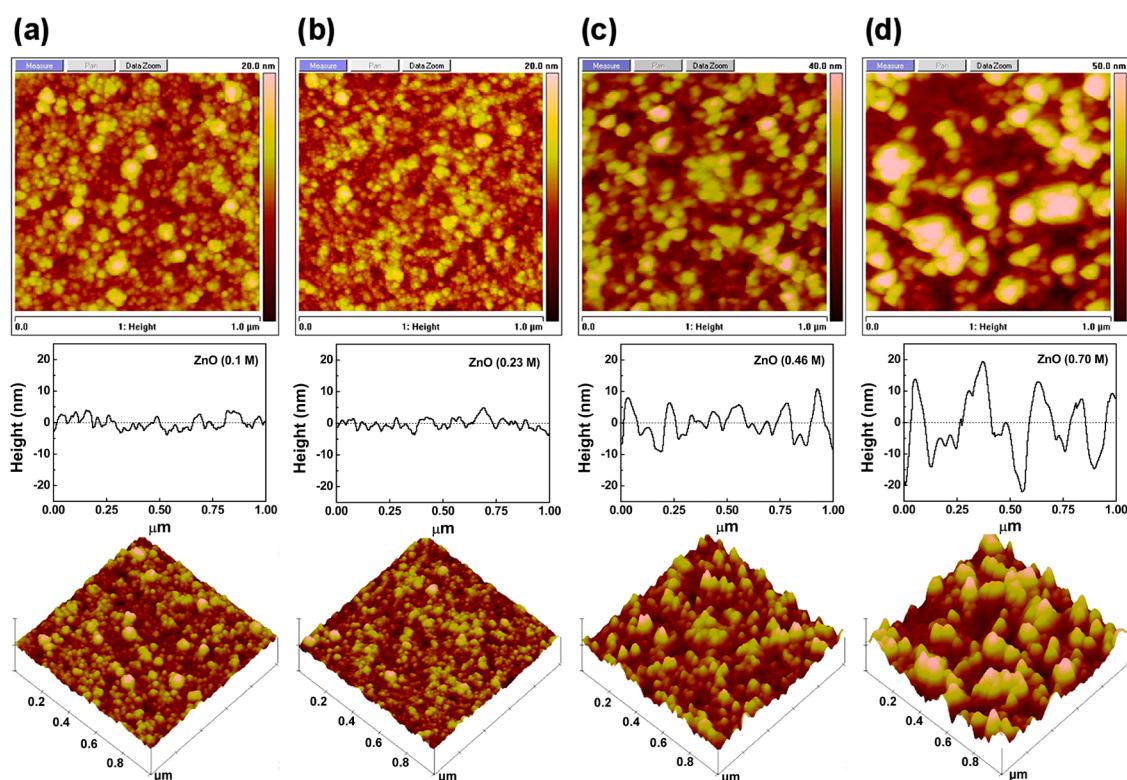
9017

dx.doi.org/10.1021/am402175m | ACS Appl. Mater. Interfaces 2013, 5, 9015−9025

Figure 2. Tapping-mode AFM images of the sol−gel ZnO films derived from different precursor solutions. Film surface morphology, surface profile, 3D topography image of (a) ZnO film (0.10 M precursor solution), (b) ZnO film (0.23 M precursor solution), (c) ZnO film (0.46 M precursor solution), and (d) ZnO film (0.7 M precursor solution).

thickness with the increasing precursor concentration. X-ray diffraction (XRD) measurements were carried out to analyze the crystallinity of the ZnO layers. No characteristic crystallization of these ZnO films is observed except for the ITO-glass background (Figure S1, shown in the Supporting Information), demonstrating the amorphous nature of the ZnO film layers. This result is in agreement with previous reports of amorphous ZnO films prepared by a sol−gel method with low temperature anealling.[28,48]

The film morphology, surface profile, and three-dimensional (3D) topography of the ZnO films were investigated by AFM. As displayed in Figure 2, uniform ZnO films composed of small nanocolloids are observed, where the grain size generally increases with the increasing precursor concentration. This behavior may be contributed to the fact that the precursor solution of a higher concentration contains a larger amount of solutes, thus increasing the probability of solutes clustering together to form larger grains.[49,50] The root mean square (RMS) roughness values are 2.39, 2.03, 5.98, and 10.71 nm for ZnO films derived from 0.10, 0.23, 0.46, and 0.70 M precursor solutions, respectively. In spite of the distinct ZnO grains similar to those of the ITO surface (see Figure S2 in the Supporting Information), it is evident that the sol−gel ZnO deposition with lower concentration precursor solutions (0.1 and 0.23 M) smooths out the ITO surface by reducing the RMS roughness from 2.87 nm for the bare ITO to less than 2.4 nm for the ZnO-modified ITO. Conversely, the higher concentration precursor solutions (0.46 and 0.70 M) can lead to coarse ZnO films with a higher RMS roughness. The results are also confirmed by the surface profiles and 3D surface topography images of the different ZnO films (Figure 2). Obviously, these ZnO films with nanoscale grains provide a

large surface area and thus can be used as efficient cathode buffer layers in the inverted PSCs for forming good electric contacts with the BHJ layer and thus improving charge collections.

Optical transmission spectra of bare ITO-glass and the ITO-glass substrates covered by sol−gel ZnO with different precursor solutions are shown in Figure 3. All four ITO/ZnO substrates show good optical transparency of over 80% average transmittance with little deviation from the bare ITO-glass. This observation suggests that the sol−gel deposition of ZnO layers on ITO cathode is not detrimental to subsequent light harvesting. Thereby, using these ZnO-modified ITO glass as
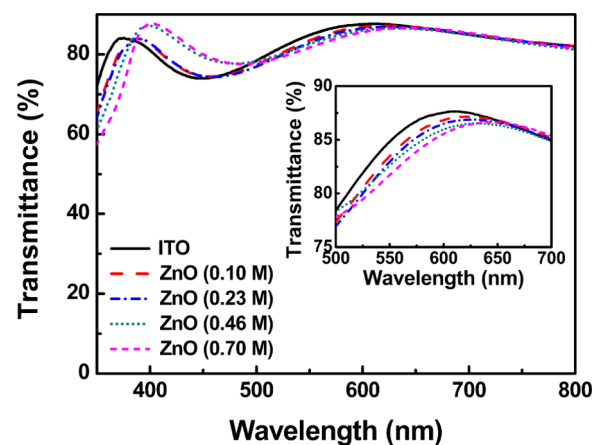

Figure 3. Optical transmission spectra of various sol−gel ZnO films fabricated on ITO-glass derived from different precursor solutions. The ITO-glass is included as a reference.

transparent cathodes could allow the maximum photon flux to reach the BHJ layer for photocurrent generation. Additionally, the film transmittance of ZnO is influenced by the precursor solutions because there is a small shift towards long wavelength with the increasing precursor concentrations. The transmittance in the range of 500−700 nm decreases with the increasing concentrations, which will affect the light harvesting of the BHJ layer, as well as the resulting device performance.

To get additional insights into these low-temperature processed ZnO films, their electron transporting properties are also investigated. The carrier mobilities were examined by the current−voltage characteristics of FETs fabricated by using ZnO as the semiconducting layer. On the basis of the transfer characteristics of the FETs (shown in Figure S3, Supporting Information), the electron mobilities in air were calculated to be 1.3×10^{-4}, 0.53×10^{-4}, 3.4×10^{-5}, and 2.6×10^{-5} cm^2 V^{-1} s^{-1} for ZnO film based devices fabricated from various precursor concentrations at 0.10, 0.23, 0.46, and 0.70 M, respectively. Although the electron-transporting properties of these low-temperature processed ZnO layers are not as good as those of crystalline ZnO films made by high temperature annealing, such electron mobilities are comparable to those of most organic materials used as electron-transporting layers.[28,48,51] Therefore, these ZnO films can serve as effective interlayers between the active layer and ITO cathode in PSCs for electron extraction and transportation. Importantly, the low-temperature processing can be potentially used for fabricating PSCs on flexible plastic substrates, which cannot withstand a high-temperature treatment. Therefore, we prepared ZnO thin-films by thermally-annealing at 200 °C. In addition, it is found that the mobility of ZnO FETs increases with decreasing concentrations of the precursor solutions although there are no obvious difference in XRD results (no crystallization, see Figure S1 in the Supporting Information). The mobility difference of these ZnO films is caused by the ZnO film thickness and morphology. Certainly, the mobility, transmittance and morphology differences of these ZnO films will affect the photovoltaic performance of the resulting inverted PSCs based on them.

To fabricate the inverted PSC devices (Figure 1b), a blend of PIFTBT8 and PC$_{71}$BM in mixed solvent without any additives was spin-coated in a glove box onto the fabricated ZnO/ITO cathode substrates. After the BHJ film was annealed, the MoO$_3$ anode buffer layer and the Ag anode were deposited. Current density−voltage (J−V) characteristics of the inverted PSCs incorporating sol−gel ZnO films derived from different precursor solutions are shown in Figure 4a. The photovoltaic parameters including PCE, V_{oc}, J_{sc}, FF, R_s, and R_{sh} are summarized in Table 1. It can be clearly seen that the device performance of the inverted PSCs is enhanced significantly by using ZnO cathode interfacial layers. The inverted device without ZnO (0 M precursor solution) as a control only produces a low PCE of 0.51% with a low V_{oc} of 0.22 V, a J_{sc} of 7.61 mA cm^{-2}, and an FF of 30.6%. After incorporating ZnO cathode interfacial layers, all of the photovoltaic parameters of inverted PSCs are remarkably improved, where the best PCE of ZnO cathode buffer layer based-devices is improved to 5.05%, with a large V_{oc} of 1.04 V, a J_{sc} of 9.74 mA cm^{-2}, and an FF of 50.1% (Figure 4a). This can be attributed to the fine-matching energy levels and the formation of good Ohmic contacts between the BHJ layer and the ITO cathode when using the ZnO buffer layer. It has been known that the CBM and VBM of ZnO (with a wide band gap of ∼3.3 eV) are about −4.4 and
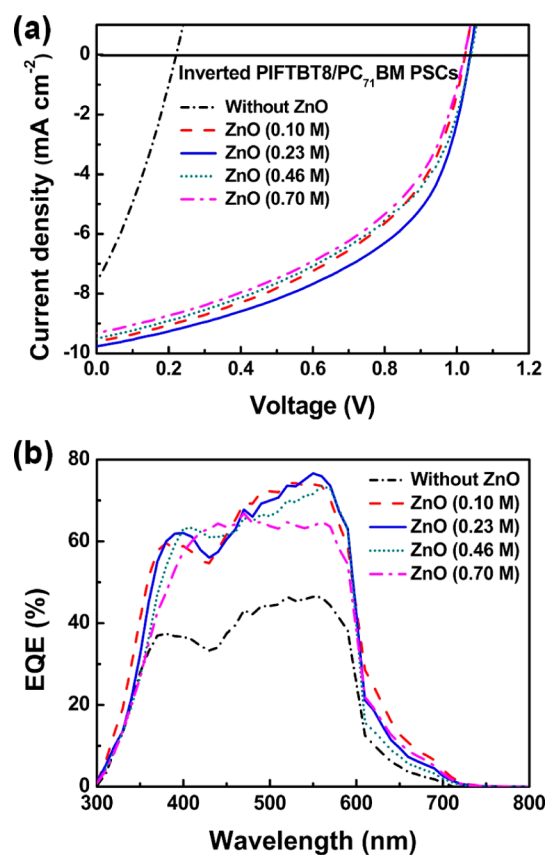

Figure 4. (a) J−V characteristics under AM 1.5 G irradiation (100 mW cm^{-2}) and (b) EQE spectra of the inverted PIFTBT8:PC$_{71}$BM PSCs with various ZnO cathode interface layers derived from different precursor solutions.

−7.7 eV, respectively.[28,45] As shown in Figure 1c, the CBM of ZnO is very close to the energy level of the LUMO of PC$_{71}$BM (∼−4.3 eV), thus electrons can be efficiently extracted by ZnO interlayers from the BHJ layer and transported to the ITO cathode through an energetically favorable pathway without a significant loss in energy. Meanwhile, the use of ZnO buffer layers circumvents the direct contact between the active layer and the cathode, and otherwise high densities of carrier traps or unfavorable interface dipoles may hinder an efficient charge collection. Using ZnO interlayers for good Ohmic contacts will maximize the V_{oc} because the reduction of built-in potential cause an increment in dark current and carrier recombination.[37] This result is also demonstrated by the corresponding J−V curves in the dark (Figure S4, see the Supporting Information). By contrast, without the use of ZnO cathode interface layer, the BHJ layer directly contacts the cathode and could not form good Ohmic contacts because the work function of ITO (∼−4.7 eV) is much deeper than the LUMO level of PC$_{71}$BM. It brings a large energy barriers formed at the interfaces thus to reduce the V_{oc} in a great extent and produces a high contact resistance.[39,52] Furthermore, without the action of ZnO cathode buffer layer, the device cannot effectively extract electrons and block holes, finally leading to a much worse device performance with an extremely small R_{sh} of 0.05 kΩ cm^2 and a large R_s of 19.7 Ω cm^2, compared to devices with ZnO cathode buffer layers.

The performance variation in the devices with various ZnO cathode interfacial layers derived from different precursor solutions is not significant in the terms of the V_{oc} (ranging from

Table 1. Device Characteristics of the Inverted PIFTBT8:PC$_{71}$BM PSCs with Various ZnO Cathode Interfacial Layers Fabricated from Different Precursor Solutions

inverted PSC device	V_{oc} (V)	J_{sc} (mA cm^{-2})	FF (%)	PCE (%) best (average^a)	R_{sh} (kΩ cm^2)	R_s (Ω cm^2)
without ZnO layer	0.22 (0.19 ± 0.03)	7.61 (7.31 ± 0.30)	30.61 (29.06 ± 1.55)	0.51 (0.41)	0.05 (0.04 ± 0.02)	19.7 (19.4 ± 0.8)
ZnO layer (0.10 M)	1.03 (1.03 ± 0.02)	9.61 (9.61 ± 0.17)	46.54 (46.21 ± 0.57)	4.60 (4.50)	0.44 (0.38 ± 0.06)	16.0 (16.1 ± 1.8)
ZnO layer (0.23 M)	1.04 (1.03 ± 0.01)	9.74 (9.70 ± 0.05)	50.11 (49.18 ± 0.93)	5.05 (4.91)	0.48 (0.47 ± 0.01)	14.4 (14.4 ± 0.5)
ZnO layer (0.46 M)	1.04 (1.02 ± 0.02)	9.49 (9.33 ± 0.16)	45.92 (45.74 ± 0.66)	4.51 (4.36)	0.40 (0.40 ± 0.03)	16.7 (19.0 ± 2.3)
ZnO layer (0.70 M)	1.02 (1.00 ± 0.02)	9.30 (9.13 ± 0.24)	46.22 (44.89 ± 1.33)	4.38 (4.10)	0.42 (0.40 ± 0.02)	18.0 (22.1 ± 4.1)

^{a}Average PCEs were based on eight devices. The R_{sh} and R_s were calculated by the inverse of the slope of the corresponding $J-V$ curves under illumination at $V = 0$ and $J = 0$, respectively.

1.02−1.04 V). This is suggested by the similar R_{sh} values ranging from 0.40 to 0.48 kΩ cm^2 (Table 1). However, prominent difference in J_{sc} and FF be clearly observed when using different ZnO cathode interfacial layers. The difference in these two parameters is determined by a balance on the optical transmittance and the possible optical spacer effects[6] and the electron mobility, as well as the morphology of ZnO films. On the whole, ZnO cathode buffer layers prepared from lower concentration sols (0.10 and 0.23 M) lead to both a larger J_{sc} and FF of the PSCs due to their higher electron mobilities, higher optical transparency and better surface morphology compared to those of ZnO buffer layers made by higher concentration sols (0.46 and 0.70 M) (Figures 2−4, and Figure S3 in the Supporting Information). The relatively large R_s, small R_{sh}, and high dark-currents are found for the devices with ZnO buffer layer fabricated from high concentration precursor solutions (0.46 and 0.70 M) (Table 1 and Supporting Information Figure S4), indicating a serious carrier recombination at the ZnO/BHJ interfaces. The large surface roughness of these ZnO buffer layers would also make the devices with thin BHJ layer susceptible to shorts and hence results in relatively small R_{sh} and FF.[31,32] On the contrary, the ZnO interface layers fabricated from lower concentration sols (0.10 and 0.23 M) not only reduce the R_s of devices owing to the good electron transfer of thinner ZnO film but also enhance the charge collection resulted from their improved morphology (smaller surface roughness and better film quality).[53] As a result, the inverted PSCs based on ZnO cathode buffer layer with 0.10, 0.23, 0.46, and 0.70 M precursor solutions exhibit maximum PCEs of 4.60%, 5.05%, 4.51%, and 4.38%, respectively, as well as the corresponding average efficiencies of 4.50%, 4.91%, 4.36%, and 4.10%, respectively. In particular, the 0.23 M precursor processed ZnO cathode interface layer produces the best performance in all of the devices, and it is a good candidate for high performance inverted PSCs due to its good balance in electron-mobility, transparency, and surface morphology.

External quantum efficiency (EQE) spectra of these inverted PSCs based on various ZnO cathode interfacial layers derived from different precursor solutions are shown in Figure 4b. It can be seen that the inverted devices using ZnO cathode interfacial layers display high EQEs across the visible region, suggesting the efficient photon-to-electron conversion processes. The inverted PSCs fabricated with lower concentration ZnO precursor sols (0.10 and 0.23 M) show larger EQE values of exceeding 70%, and the devices made by higher concentration ZnO precursor sols (0.46 and 0.70 M) exhibit medium EQE values of 65−70%. Whereas the PSCs without a ZnO cathode buffer layer have the lowest EQE value (∼46%).

The EQE values are consistent with the trend of J_{sc} measured in the corresponding PSC devices.

Moreover, a higher V_{oc} or J_{sc} for the inverted PSCs can be obtained by fine tuning the BHJ layer based on the optimized device configuration of ITO/ZnO(0.23 M)/BHJ layer/MoO$_3$/Ag. We adjusted the BHJ layer thickness from 86 to 66 nm by varying spin rates from 800 to 1200 rpm. Figure 5 provides $J-V$
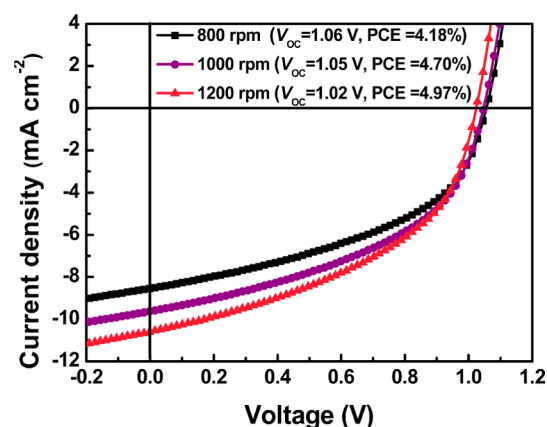

Figure 5. $J-V$ curves of the inverted ITO/ZnO(0.23 M)/PIFTBT8:PC$_{71}$BM/MoO$_3$/Ag devices with different BHJ layers prepared by different spin speeds.

curves of these inverted PSCs fabricated by different spin rates. When the spin speed changes from 1100 to 1000 rpm (a BHJ layer thickness from 71 to 75 nm), the V_{oc} increases from 1.04 to 1.05 V with a comparable PCE of 4.70%. A further improved V_{oc} as high as 1.06 V with a PCE of 4.18% is obtained by using a lower spin rate (800 rpm). In contrast, a thinner BHJ layer made by increasing the spin rate to 1200 rpm, produces a higher J_{sc} exceeding 10 mA cm^{-2} and retains a PCE of 4.97% and a V_{oc} of 1.02 V. Notably, these large V_{oc} values (1.02−1.06 V) with high PCEs (4.2−5.1%) for the inverted PSCs are better than those of reported regular PSCs.[54,55] We realize that the fill factors of these inverted devices are still not high (most of them are <50%), and the photocurrents in reverse bias exhibit a mild field-dependence due to the field dependent exciton dissociation rate, and thus reducing FFs.[46] Incorporation of solvent additives such as 1,8-diiodooctane or 1-chloronaphthalene for the BHJ layer processing can be further used to modulate the phase-separation morphology and to improve the BHJ film quality as well as its connections with the electrodes, thus increasing the FF.[12,55] Therefore, there should be good chances to further optimize the device performance by fine-tuning the fabrication conditions, by introducing suitable solvent additives, or by carefully engineering every layer within devices to

9020

dx.doi.org/10.1021/am402175m | ACS Appl. Mater. Interfaces 2013, 5, 9015−9025

minimize the R_s and dark-current while enlarge the R_{sh} throughout the inverted PSCs.

Optimization of Different Metal Oxide Anode Interfacial Layers such as MoO_3 to Improve Device Performance. Apart from the impact of the ZnO cathode buffer layer, the MoO_3 anode interfacial layer also plays a significant role in determining the photovoltaic performance of the inverted PSCs. We fabricated a series of inverted devices based on the ZnO cathode interlayer (with a 0.23 M precursor solution) and the anode buffer layer of thermally-deposited MoO_3 films with different thicknesses. Figure 6 compares the dependence of V_{oc},
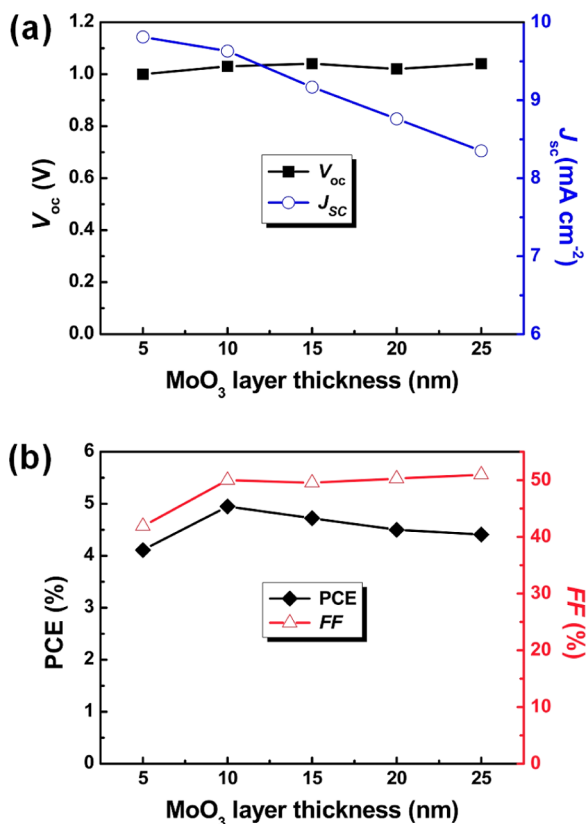

Figure 6. Photovoltaic parameters of the inverted solar cells based on PIFTBT8:PC$_{71}$BM are plotted as functions of the thickness of MoO_3 anode interfacial layer: (a) V_{oc} (■) and J_{sc} (○) versus MoO_3 layer thickness and (b) PCE (♦) and FF (△) versus MoO_3 layer thickness.

J_{sc}, FF, and PCE of inverted PSCs on MoO_3 thickness. It can be seen that, the device performance largely depends on the variation of MoO_3 layer thickness. When the thickness of MoO_3 layer is varied between 10 nm and 20 nm, all devices exhibit a high V_{oc} in the range of 1.02−1.04 V and a comparable FF of ∼50%. However, with reducing the thickness of MoO_3 layer to 5 nm, the V_{oc} and the FF drop to 1.00 V and 41.9%, respectively. By contrast, an increase of the MoO_3 layer thickness to 25 nm leads to a higher V_{oc} (1.04 V) and a larger FF (∼51%). As to the J_{sc}, conversely, it decreases gradually with the increasing MoO_3 thickness (Figure 6a), which demonstrates that the MoO_3 anode buffer layer affects the hole-extraction and transportation. For example, the highest J_{sc} of 9.81 mA cm^{-2} is obtained at the condition of 5 nm MoO_3, while the lowest J_{sc} of 8.35 mA cm^{-2} for the 25 nm MoO_3. It is noted that the PCEs are directly determined by J_{sc}, V_{oc}, and FF, and a balance among them will afford the best PCE. As a result,

the highest PCE of 4.95% (with a 4.85% average efficiency) of this type of inverted PSCs are finally obtained with a 10 nm of MoO_3 interlayer (Figure 6b). Other inverted devices with 5, 15, 20, and 25 nm MoO_3 anode interfacial layer exhibit PCEs of 4.11%, 4.72%, 4.50%, and 4.41%, respectively, as well as the average efficiencies of 4.03%, 4.64%, 4.46%, and 4.21%, respectively. To further understand the reasons for the variation in V_{oc}, J_{sc}, and FF as well as PCE caused by the thickness of MoO_3 anode interlayer, the R_s and R_{sh} associated with the device parameters are summarized in Supporting Information Table S1. We can see that the R_s increases from 13.7 Ω cm^2 to 14.0, 14.3, 15.2, and 17.2 Ω cm^2 with the increase of the MoO_3 thickness from 5 to 10, 15, 20, and 25 nm, respectively. This is in good agreement with the trends of J_{sc} values, thus echoing the photocurrent changes in devices with MoO_3 anode interfacial layers of different thicknesses. Despite the fact that the smallest R_s is achieved for the devices with 5 nm MoO_3, nonetheless, the corresponding R_{sh} is only 0.30 kΩ cm^2 which hinders the creation of a large V_{oc} as well as a high FF due to the poor film quality of this ultrathin MoO_3 layer and the negative effects as an optical spacer for devices,[56,57] finally leading to the lowest PCE of 4.11%. By contrast, the device with a thicker MoO_3 film (10 nm) produces a much higher R_{sh} of 0.47 kΩ cm^2 thus giving rise to increased V_{oc} as well as FF, and finally, an improved PCE of 4.95%. To further increase the thickness of MoO_3 layer to 15−25 nm, the R_{sh} can maintain a high level of 0.45−0.49 kΩ cm^2 which contributes to higher values in V_{oc}, FF, and PCEs compared to the device with 5 nm MoO_3 layer. However, the PCEs of devices are lower than the device with 10 nm MoO_3, mainly due to their low J_{sc} values induced by large R_s.

Besides the MoO_3 anode buffer layers, other semiconducting transition metal oxides such as WO_3, NiO, and Cu_2O are also investigated in this work as hole-extracting anode interfacial layers to fabricate inverted solar cells. Figure 7 shows the $J−V$ characteristics measured under illumination and in the dark for the inverted devices with different metal oxide anode interfacial layers. And, Table 2 summaries the corresponding photovoltaic parameters for these inverted PSCs. In the case of using bare Ag anode without any buffer layers, the inverted devices do not exhibit any diode characteristics. This is not surprising because there are very poor electric contacts and a large Schottky barrier forms between Ag (work-function ∼ −4.6 eV) and PIFTBT8 (HOMO ∼ −5.5 eV), which is unfavorable for hole collection.[39] When using thermally-deposited p-type NiO as an anode buffer layer, an optimized device exhibits a diode characteristic and produces a PCE of 0.81% with a low V_{oc} of 0.32 V, a J_{sc} of 6.12 mA cm^{-2}, and an FF of 40.76%. This low PCE is mainly induced by the low V_{oc}, which is also demonstrated by its low R_{sh} (∼0.15 kΩ cm^2) and the large dark-current.[37] By employing vacuum-deposited Cu_2O as an anode buffer layer, the inverted device shows an increased R_{sh} of 0.23 kΩ cm^2 and thus obtains a higher V_{oc} of 0.46 V and a better PCE of 1.18%. In the case of using WO_3 as anode interfacial layers, devices with enhanced performance are obtained. The optimized device exhibits a 2.50% PCE with a V_{oc} of 0.65 V, a J_{sc} of 8.80 mA cm^{-2}, and an FF of 43.7%, which are much better than those of the devices with NiO and Cu_2O anode buffer layers. In addition, the descending order of dark-currents for the devices with NiO, Cu_2O, WO_3 and MoO_3 layers is mainly due to the built-in voltage shifting and the leakage current suppression by using different metal oxide anode interfacial layers besides their differences in electrical
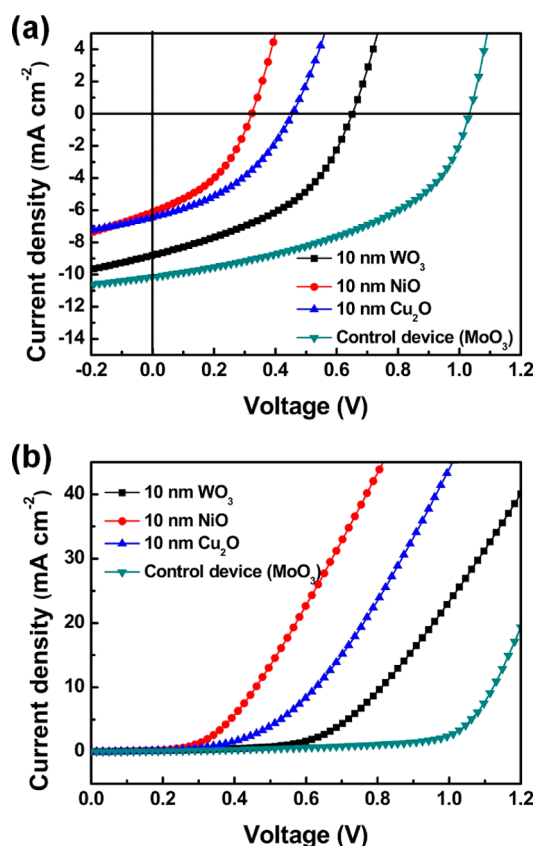
Figure 7. $J-V$ curves of inverted PIFTBT8:PC$_{71}$BM PSCs with different metal oxide anode interfacial layers: (a) under AM 1.5 G illumination (100 mW cm^{-2}) and (b) in the dark.

characteristics of the device interfaces.[58] The results demonstrate the important role of anode buffer layers in determining the performance of the inverted PSCs.

The different performance of these inverted PSCs using various metal oxide anode interfacial layers may be ascribed to their differences in the energy levels, as well as their energy-matching conditions or interfacial contacts with the BHJ materials and the metallic anode. It has been reported that the VBM and the CBM of the MoO$_3$ film are ~−5.3 and −2.3 eV, respectively.[59] As displayed in Figure 1c, because the VBM of MoO$_3$ is well matched with the HOMO level of the PIFTBT8 (~−5.5 eV), thus the effective extraction and transportation of holes to Ag anode through the MoO$_3$ interlayer is expected. Compared to MoO$_3$, the VBM value of the NiO anode interlayer (~−5.0 eV) is much higher than the HOMO of PIFTB8,[36,60] which indicates the existence of a large energy gap. It thus causes poor electric contacts and forms large energy barriers, leading to a low photocurrent and a reduced built-in potential as well as a consequently low PCE. These results are

also reflected by the high R_s, low R_{sh} and large dark-currents for the inverted devices with the NiO anode buffer layer. In the case of Cu$_2$O, its VBM value (~−5.2 eV) is larger than the VBM of NiO; nevertheless, the higher CBM of Cu$_2$O (~−3.1 eV) is relatively close to the LUMO of PIFTBT8 (−3.5 eV), possibly resulting in a bad electron blocking.[61] Thus, the corresponding devices did not show a good device performance similar to that of the devices with the NiO interlayer. By contrast, the device with WO$_3$ buffer layer, although its VBM value (−5.1 eV) is not very close to the HOMO of PIFTBT8, the smallest CBM (−1.6 eV) in these metal oxide layers is much higher than the LUMOs of PIFTBT8 and PC$_{71}$BM.[62] This provides a way to efficiently block electrons from the active layer, thus contributing to higher J_{sc} and V_{oc} than those of the devices with Cu$_2$O and NiO anode interlayers, giving an encouraging PCE of 2.5%. Accordingly, choosing well energy-matching anode buffer layers between active materials and electrodes, as well as the nature of contacts at the interfaces is one of the most effective strategies to improve the performance of the inverted PSCs.

Solar Cell Device Stability. Besides high efficiency, long-term device stability is also a particularly important property for organic solar cells. Therefore, there is a need to examine the stability of these inverted PSCs. Incorporation of semiconducting metal oxide interlayers into PSCs with inverted device configurations has been proven as an efficient strategy to enhance the device stability and lifetime. The device stability of the inverted PSCs with various ZnO cathode interfacial layers derived from different precursor solutions as a function of storage time under ambient conditions is shown in Figure 8. All the inverted PSCs with ZnO cathode interfacial layers exhibit good device stability, and their PCEs can maintain at approximately >90% of their original values even after storage in air for 180 days. Both V_{oc} and FF over this long period remain relatively constant with slightly decreased J_{sc}, leading to normalized PCEs with a small degradation. Thus, the best inverted device still exhibit good photovoltaic performance with a high PCE of 4.55%, a large V_{oc} of 1.05 V, a J_{sc} of 9.08 mA cm^{-2}, and an FF of 47.8% after 180 days. The corresponding R_{sh} and R_s values (0.45 kΩ cm^2 and 19.8 Ω cm^2, respectively) are comparable to the initial values, which reconfirm the device stability. In contrast, the inverted PSC without ZnO interlayer shows relatively poor stability. Its PCE value decayed to less than 70% of its initial efficiency after air exposure for only 20 days and further decayed to 35% after the storage in air for 180 days. Compared to inverted PSCs with/without ZnO interlayers, the regular PSC device with the anode of PEDOT:PSS-modified ITO and the LiF/Al cathode exhibited a more than 50% decrease in PCE after storage for 20 days, and a more than 70% decrease in PCE after 35 days. Similarly, other conventional PSCs using MoO$_3$-modified ITO as the anode and LiF/Al (or Ca/Al) as the cathode also showed a serious

Table 2. Device Characteristics of the Inverted PIFTBT8:PC$_{71}$BM PSCs with Different Transition Metal Oxide Anode Interlayers

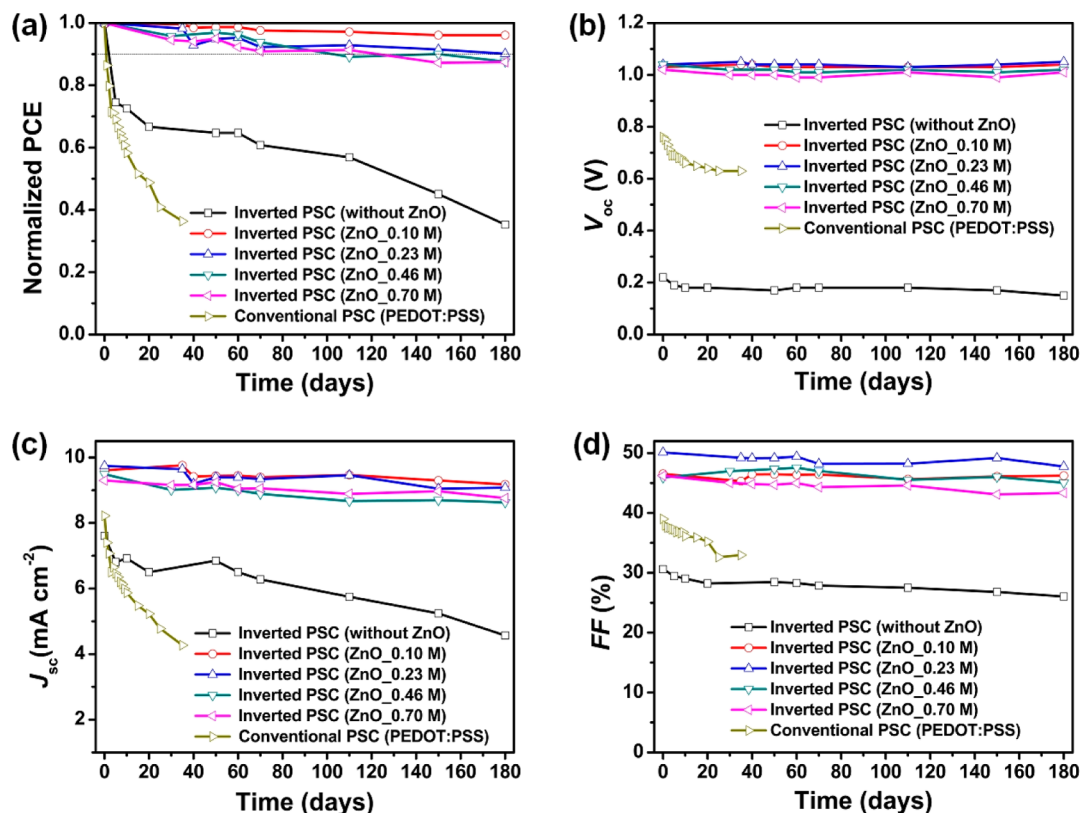| inverted PSC device	V_{oc} (V)	J_{sc} (mA cm^{-2})	FF (%)	PCE (%) best (average)	R_{sh} (kΩ cm^2)	R_s (Ω cm^2)
10 nm WO$_3$	0.65	8.80	43.71	2.50 (2.37)	0.21	21.0
10 nm NiO	0.32	6.12	40.76	0.81 (0.68)	0.15	18.9
10 nm Cu$_2$O	0.46	6.45	40.16	1.18 (1.01)	0.23	27.2
control device (MoO$_3$)	1.03	10.10	45.50	4.74 (4.64)	0.38	15.9

Figure 8. Device performance of the inverted and conventional PIFTBT8:PC$_{71}$BM based solar cells stored for 180 days in air under ambient conditions: (a) normalized PCE, (b) V_{oc}, (c) J_{sc}, and (d) FF.

degradation in photovoltaic performance (Figure S5, in the Supporting Information), illustrating an inferior device reliability to that of the inverted PSCs. Accordingly, the use of ZnO films as the cathode interfacial layers in inverted solar cells yields a significant improvement in long-term device stability, which is much better than that of the inverted PSCs without ZnO as well as that of various conventional devices. We also explored the stability of the inverted PSCs with different metal oxide anode interfacial layers. As shown in Figure S6 (see the Supporting Information), all the photovoltaic parameters of the inverted devices are stable with negligible degradation. The normalized PCEs can remain over 90% after storage in air for two months.

The inverted PSCs using transition metal oxide cathode/anode interfacial layers demonstrate much better device stability than that of the conventional PSCs. The improved stability is attributed to the use of both the transition metal oxide interfacial layers and the Ag electrode. The incorporation of transition metal oxides on both sides of the active layer prevents the diffusion of moisture and oxygen into the BHJ layer, thereby enhancing the device stability. In addition, the high-work function Ag anode is stable in air which can serve as a protective cover to improve the stability of devices. By contrast, the conventional PSCs undergo serious degradation owing to the high reactivity of low work-function Al or Ca cathode with moisture and oxygen, and the acidic nature of PEDOT:PSS interlayer which will react with ITO.[20−22] The improved long-term lifetime of these inverted PSCs opens a promising way to fabricate PSC products with comparable stability to that of the currently dominant solar cells. It is expected that the device stability and lifetime could be further improved by the use of some more advanced encapsulation technologies for organic solar cells.

■ CONCLUSIONS

In summary, we fabricated and demonstrated a series of inverted BHJ solar cells with high V_{oc} of 1.00−1.06 V based on a PIFTBT8:PC$_{71}$BM blend and transition metal oxide based cathode/anode interlayers. Interface control of low-temperature solution processed ZnO films as cathode interfacial layers and various metal oxide thin-films as anode buffer layers provides effective charge extraction and transportation, leading to the efficient inverted PSCs with excellent device stability. Incorporation of optimized metal oxide interlayers can reduce interfacial power losses thus affords improved device performance. As a result of improved interface contacts and fine-matching energy levels in an optimized interface condition, a high PCE of 5.05% with a large V_{oc} up to 1.04 V, a J_{sc} of 9.74 mA cm^{-2}, and an FF of 50.1% was achieved. To the best of our knowledge, this is the first example of single junction inverted PSC over 5% PCE with a V_{oc} approaching 1.05 V. Additionally, the highest PCE of the inverted PSCs remains >90% of its initial value (a PCE of 4.55% with a V_{oc} of 1.05 V) over 6 months, demonstrating good long-term stability when compared to the conventional PSCs. Our results highlight the important role of metal oxide cathode/anode interface layers in determining the device photovoltaic parameters such as V_{oc}, J_{sc}, FF, R_s, R_{sh}, as well as PCE and stability. The results also demonstrate that the interface engineering of metal oxide interlayers is a significant and promising strategy to develop efficient and stable PSCs with a high V_{oc}.

ASSOCIATED CONTENT

Ⓢ Supporting Information

XRD results of ZnO films, AFM image of the ITO surface, transfer characteristics of FETs with ZnO films, dark-current curves of inverted PSCs, photovoltaic performance of inverted devices with different MoO_3 anode buffer layers, and device stability of conventional and inverted PSCs. This material is available free of charge via the Internet at http://pubs.acs.org.

AUTHOR INFORMATION

Corresponding Author
*E-mail: qingdongzheng@fjirsm.ac.cn.

Notes
The authors declare no competing financial interest.

ACKNOWLEDGMENTS

REFERENCES

(1) Barnham, K. W. J.; Mazzer, M.; Clive, B. *Nat. Mater.* **2006**, *5*, 161−164.

(2) Chu, S.; Majumdar, A. *Nature* **2012**, *488*, 294−303.

(3) Brabec, C. J.; Sariciftci, N. S.; Hummelen, J. C. *Adv. Funct. Mater.* **2001**, *11*, 15−26.

(4) Li, G.; Zhu, R.; Yang, Y. *Nat. Photonics* **2012**, *6*, 153−161.

(5) Girotto, C.; Voroshazi, E.; Cheyns, D.; Heremans, P.; Rand, B. P. *ACS Appl. Mater. Interfaces* **2011**, *3*, 3244−3247.

(6) Gilot, J.; Barbu, I.; Wienk, M.M.; Janssen, R.A. *Appl. Phys. Lett.* **2007**, *91*, 113520.

(7) Sariciftci, N. S.; Smilowitz, L.; Heeger, A. J.; Wudl, F. *Science* **1992**, *258*, 1474−1476.

(8) Halls, J. J. M.; Walsh, C. A.; Greenham, N. C.; Marseglia, E. A.; Friend, R. H.; Moratti, S. C.; Holmes, A. B. *Nature* **1995**, *376*, 498−500.

(9) Liang, Y.; Yu, L. *Acc. Chem. Res.* **2010**, *43*, 1227−1236.

(10) Chu, T. -Y.; Lu, J. P.; Beaupré, S.; Zhang, Y. G.; Pouliot, J. R.; Wakim, S.; Zhou, J. Y.; Leclerc, M.; Li, Z.; Ding, J. F.; Tao, Y. *J. Am. Chem. Soc.* **2011**, *133*, 4250−4253.

(11) He, Z.; Zhong, C.; Su, S.; Xu, M.; Wu, H.; Cao, Y. *Nat. Photonics* **2012**, *6*, 591−595.

(12) Guo, X.; Cui, C.; Zhang, M.; Huo, L.; Huang, Y.; Hou, J.; Li, Y. *Energy Environ. Sci.* **2012**, *5*, 7943−7949.

(13) Dou, L.; You, J.; Yang, J.; Chen, C. -C.; He, Y.; Murase, S.; Moriarty, T.; Emery, K.; Li, G.; Yang, Y. *Nat. Photonics* **2012**, *6*, 180−185.

(14) You, J.; Dou, L.; Yoshimura, K.; Kato, T.; Ohya, K.; Moriarty, T.; Emery, K.; Chen, C.-C.; Gao, J.; Li, G.; Yang, Y. *Nat. Commun.* **2013**, *4*, 1446.

(15) Cai, D.; Zheng, Q.; Chen, S.-C.; Zhang, Q.; Lu, C.-Z.; Sheng, Y.; Zhu, D.; Yin, Z.; Tang, C. *J. Mater. Chem.* **2012**, *22*, 16032−16040.

(16) Green, M. A.; Emery, K.; Hishikawa, Y.; Warta, W.; Dunlop, E. D. *Prog. Photovoltaics* **2012**, *20*, 12−20.

(17) Yu, G.; Gao, J.; Hummelen, J. C.; Wudl, F.; Heeger, A. J. *Science* **1995**, *270*, 1789−1791.

(18) Shaheen, S. E.; Brabec, C. J.; Sariciftci, N. S.; Padinger, F.; Fromherz, T.; Hummelen, J. C. *Appl. Phys. Lett.* **2001**, *78*, 841−843.

(19) Ma, W.; Yang, C.; Gong, X.; Lee, K.; Heeger, A. J. *Adv. Funct. Mater.* **2005**, *15*, 1617−1622.

(20) Yin, Z.; Zheng, Q. *Adv. Energy Mater.* **2012**, *2*, 179−218.

(21) Kawano, K.; Pacios, R.; Poplavskyy, D.; Nelson, J.; Bradley, D. D. C.; Durrant, J. R. *Sol. Energy Mater. Sol. Cells* **2006**, *90*, 3520−3530.

(22) Jorgensen, M.; Norrman, K.; Gevorgyan, S. A.; Tromholt, T.; Andreasen, B.; Krebs, F. C. *Adv. Mater.* **2012**, *24*, 580−612.

(23) Amb, C. M.; Chen, S.; Graham, K. R.; Subbiah, J.; Small, C. E.; So, F.; Reynolds, J. R. *J. Am. Chem. Soc.* **2011**, *133*, 10062−10065.

(24) Li, Y. *Acc. Chem. Res.* **2012**, *45*, 723−733.

(25) You, J.; Li, X.; Xie, F.; Sha, W. E. I.; Kwong, J. H. W.; Li, G.; Choy, W. C. H.; Yang, Y. *Adv. Energy Mater.* **2012**, *2*, 1203−1207.

(26) Ma, H.; Yip, H.-L.; Huang, F.; Jen, A. K.-Y. *Adv. Funct. Mater.* **2010**, *20*, 1371−1388.

(27) Po, R.; Carbonera, C.; Bernardi, A.; Camaioni, N. *Energy Environ. Sci.* **2011**, *4*, 285−310.

(28) Sun, Y.; Seo, J. H.; Takacs, C. J.; Seifter, J.; Heeger, A. J. *Adv. Mater.* **2011**, *23*, 1679−1683.

(29) Zou, J.; Yip, H.-L.; Zhang, Y.; Gao, Y.; Chien, S.-C.; O'Malley, K.; Chueh, C.-C.; Chen, H.; Jen, A. K.-Y. *Adv. Funct. Mater.* **2012**, *22*, 2804−2811.

(30) Chen, S.; Small, C. E.; Amb, C. M.; Subbiah, J.; Lai, T.-H.; Tsang, S.-W.; Manders, J. R.; Reynolds, J. R.; So, F. *Adv. Energy Mater.* **2012**, *2*, 1333−1337.

(31) Liu, J.; Shao, S.; Meng, B.; Fang, G.; Xie, Z.; Wang, L.; Li, X. *Appl. Phys. Lett.* **2012**, *100*, 213906.

(32) Manor, A.; Katz, E. A.; Tromholt, T.; Krebs, F. C. *Adv. Energy Mater.* **2011**, *1*, 836−843.

(33) Small, C. E.; Chen, S.; Subbiah, J.; Amb, C. M.; Tsang, S. W.; Lai, T. H.; Reynolds, J. R.; So, F. *Nat. Photonics* **2012**, *6*, 115−120.

(34) Yang, T.; Wang, M.; Duan, C.; Hu, X.; Huang, L.; Peng, J.; Huang, F.; Gong, X. *Energy Environ. Sci.* **2012**, *5*, 8208−8214.

(35) Vandewal, K.; Tvingstedt, K.; Gadisa, A.; Inganäs, O.; Manca, J. V. *Nat. Mater.* **2009**, *8*, 904−909.

(36) Irwin, M. D.; Buchholz, B.; Hains, A. W.; Chang, R. P. H.; Marks, T. J. *Proc. Natl. Acad. Sci. U.S.A.* **2008**, *105*, 2783−2787.

(37) Chen, S.; Manders, J. R.; Tsang, S.-W.; So, F. *J. Mater. Chem.* **2012**, *22*, 24202−24212.

(38) Blom, P. W. M.; Mihailetchi, V. D.; Koster, L. J. A.; Markov, D. E. *Adv. Mater.* **2007**, *19*, 1551−1566.

(39) Yip, H. L.; Hau, S. K.; Baek, N. S.; Ma, H.; Jen, A. K.-Y. *Adv. Mater.* **2008**, *20*, 2376−2382.

(40) Moliton, A.; Nunzi, J. M. *Polym. Int.* **2006**, *55*, 583−600.

(41) Yip, H.-L.; Jen, A. K.-Y. *Energy Environ. Sci.* **2012**, *5*, 5994−6011.

(42) Cai, W.; Gong, X.; Cao, Y. *Sol. Energy Mater. Sol. Cells* **2010**, *94*, 114−127.

(43) Krebs, F. C. *Sol. Energy Mater. Sol. Cells* **2009**, *93*, 394−412.

(44) He, Z.; Zhong, C.; Huang, X.; Wong, W.-Y.; Wu, H.; Chen, L.; Su, S.; Cao, Y. *Adv. Mater.* **2011**, *23*, 4636−4643.

(45) Huang, J.; Yin, Z.; Zheng, Q. *Energy Environ. Sci.* **2011**, *4*, 3861−3877.

(46) Zheng, Q.; Jung, B. J.; Sun, J.; Katz, H. E. *J. Am. Chem. Soc.* **2010**, *132*, 5394−5404.

(47) Foong, T. R. B.; Singh, S. P.; Sonar, P.; Ooi, Z.-E.; Chan, K. L.; Dodabalapur, A. *J. Mater. Chem.* **2012**, *22*, 20896−20901.

(48) Yang, T.; Cai, W.; Qin, D.; Wang, E.; Lan, L.; Gong, X.; Peng, J.; Cao, Y. *J. Phys. Chem. C* **2010**, *114*, 6849−6853.

(49) O'Brien, S.; Koh, L. H. K.; Crean, G. M. *Thin Solid Films* **2008**, *516*, 1391−1395.

(50) Kyaw, A. K. K.; Sun, X. W.; Jiang, C. Y.; Lo, G. Q.; Zhao, D. W.; Kwong, D. L. *Appl. Phys. Lett.* **2008**, *93*, 221107.

(51) Nelson, J.; Kwiatkowski, J. J.; Kirkpatrick, J.; Frost, J. M. *Acc. Chem. Res.* **2009**, *42*, 1768−1778.

(52) Yip, H.-L.; Hau, S. K.; Baek, N. S.; Jen, A. K.-Y. *Appl. Phys. Lett.* **2008**, *92*, 193313.

(53) Li, G.; Shrotriya, V.; Huang, J.; Yao, Y.; Moriarty, T.; Emery, K.; Yang, Y. *Nat. Mater.* **2005**, *4*, 864−868.

(54) Hoke, E. T.; Vandewal, K.; Bartelt, J. A.; Mateker, W. R.; Douglas, J. D.; Noriega, R.; Graham, K. R.; Fréchet, J. M. J.; Salleo, A.; McGehee, M. D. *Adv. Energy Mater.* **2013**, *3*, 220−230.

(55) Yuan, J.; Zhai, Z.; Dong, H.; Li, J.; Jiang, Z.; Li, Y.; Ma, W. *Adv. Funct. Mater.* **2013**, *23*, 885−892.

(56) Sun, Y.; Takacs, C. J.; Cowan, S. R.; Seo, J. H.; Gong, X.; Roy, A.; Heeger, A. J. *Adv. Mater.* **2011**, *23*, 2226−2230.

(57) Zhao, D. W.; Tan, S. T.; Ke, L.; Liu, P.; Kyaw, A. K. K.; Sun, X. W.; Lo, G. Q.; Kwong, D. L. *Sol. Energy Mater. Sol. Cells* **2010**, *94*, 985−991.

(58) He, C.; Zhong, C.; Wu, H.; Yang, R.; Yang, W.; Huang, F.; Bazan, G. C.; Cao, Y. *J. Mater. Chem.* **2010**, *20*, 2617−2622.

(59) Shrotriya, V.; Li, G.; Yao, Y.; Chu, C.-W.; Yang, Y. *Appl. Phys. Lett.* **2006**, *88*, 073508.

(60) Shim, W. H.; Park, S.-Y.; Park, M. Y.; Seo, H. O.; Kim, K.-D.; Kim, Y. T.; Kim, Y. D.; Kang, J.-W.; Lee, K. H.; Jeong, Y.; Lim, D. C. *Adv. Mater.* **2011**, *23*, 519−522.

(61) Lin, M.-Y.; Lee, C.-Y.; Shiu, S.-C.; Wang, I.-J.; Sun, J.-Y.; Wu, W.-H.; Lin, Y.-H.; Huang, J.-S.; Lin, C.-F. *Org. Electron.* **2010**, *11*, 1828−1834.

(62) Han, S.; Shin, W. S.; Seo, M.; Gupta, D.; Moon, S.-J.; Yoo, S. *Org. Electron.* **2009**, *10*, 791−797.